

# One-Dimensional Cluster Growth and Branching Gels in Colloidal Systems with Short-Range Depletion Attraction and Screened Electrostatic Repulsion

F. Sciortino,<sup>†</sup> P. Tartaglia,<sup>‡</sup> and E. Zaccarelli<sup>\*,†,§</sup>

Dipartimento di Fisica and INFM-CRS-SOFT, Università di Roma La Sapienza, P. le A. Moro 2, 00185 Roma, Italy, Dipartimento di Fisica and INFM-CRS-SMC, Università di Roma La Sapienza, P. le A. Moro 2, 00185 Roma, Italy, and ISC-CNR, Via del Taurini 19, 00185 Roma, Italy

Received: May 22, 2005; In Final Form: August 11, 2005

We report extensive numerical simulations of a simple model for charged colloidal particles in suspension with small nonadsorbing polymers. The chosen effective one-component interaction potential is composed of a short-range attractive part complemented by a Yukawa repulsive tail. We focus on the case where the screening length is comparable to the particle radius. Under these conditions, at low temperature, particles locally cluster into quasi one-dimensional aggregates which, via a branching mechanism, form a macroscopic percolating gel structure. We discuss gel formation and contrast it with the case of longer screening lengths, for which previous studies have shown that arrest is driven by the approach to a Yukawa glass of spherical clusters. We compare our results with recent experimental work on charged colloidal suspensions (*Phys. Rev. Lett.* **2005**, *94*, 208301).

## I. Introduction

Recent years have witnessed a progressive interest in the role of the interparticle potential on controlling structure and dynamics of colloidal dispersions. Experiments,<sup>1–12</sup> theory,<sup>13–15</sup> and simulation<sup>16–21</sup> studies have provided evidence that when the hard-core repulsion is complemented simultaneously by a short range attraction (of finite depth) and by a screened electrostatic repulsion, particles tend to form aggregates, whose shape and size is sensitively dependent on the balance between attraction and repulsion.<sup>22–26,20,27</sup> In some cases, the system shows an equilibrium cluster phase, where particles associate and dissociate reversibly into clusters.<sup>4,10,11</sup> Interestingly enough, these cluster phases appear not only in colloidal systems but also in protein solutions, at the limit of low salt concentration.<sup>4,5,12</sup> Estimates of the ground-state configuration of isolated clusters of different size<sup>20</sup> suggest that, when the clusters diameter exceeds the screening length, the shape of the aggregates crosses from spherical to linear. Evidence has been reported that, for appropriate tuning of the external control parameters, colloidal cluster phases progressively evolve toward an arrested state.<sup>1,7,10,12</sup> Recent numerical studies suggest that arrest may be connected to a percolation process.<sup>17,18</sup> A different arrest scenario has been proposed, and supported by numerical simulations, for the case of relatively large screening length (i.e., the case of preferentially spherical clusters), dynamic arrest may proceed via a glass transition mechanism, where clusters, acting as *superparticles* interacting via a renormalized Yukawa potential, become confined by the repulsions created by their neighboring clusters.<sup>16</sup> This mechanism is, in all respects, identical to the glass transition of Yukawa particles<sup>28–31</sup> and leads, favored by the intrinsic polydispersity of the clusters induced by the growth process, to the realization of a Wigner

glass. The simulation study<sup>16</sup> showed that the resulting arrested state is not percolating; i.e., the arrest transition cannot be interpreted in terms of the formation of a bonded network of particles.

A very recent experimental work<sup>7</sup> has reported evidence of arrest via linear cluster growth followed by percolation, in a system of charged colloidal particles. In the studied system, the short-range attraction, induced via depletion mechanism, is complemented by an electrostatic repulsion, with a Debye screening length  $\xi$  estimated on the order of  $\xi/\sigma \approx 0.65$ , where  $\sigma$  indicates the hard core diameter of the colloidal particle. The quasi one-dimensional clusters observed via confocal microscopy are locally characterized by a Bernal spiral geometry,<sup>32</sup> the same structure found as cluster ground-state configuration for the case of screening lengths smaller than  $\sigma$ .<sup>20</sup> The Bernal spiral, shown in Figure 1, is composed of face sharing tetrahedra, in which each particle is connected to six neighbors.

In this work, we numerically investigate the possibility that, when the potential parameters are such that the Bernal spiral is the ground-state structure for isolated clusters, macroscopic gels can be formed at large, but finite, attraction strength, via a mechanism of branching favored by the small but finite thermal contributions. We explore the low packing fraction region for several values of the attractive interaction strength, to highlight the collective effects arising from cluster–cluster interactions and to assess under which external conditions, ground state predictions are valid. We carry our study along two routes. In both cases, we study a colloid–polymer mixture in the effective one-component description, i.e., assuming that the polymer size is much smaller than that of the colloids. In the first route, we control the attraction between colloidal particles via a temperature scale. In the second route—designed to make direct contact with the experimental work reported in ref 7—we study an isothermal system where the repulsive part of the potential is fixed, while the attractive part of the potential is varied according to the concentration of depletant, to model the strength of the polymer-induced depletion interaction. We will refer to these

<sup>†</sup> Dipartimento di Fisica and INFM-CRS-SOFT, Università di Roma La Sapienza.

<sup>‡</sup> Dipartimento di Fisica and INFM-CRS-SMC, Università di Roma La Sapienza.

<sup>§</sup> ISC-CNR.



**Figure 1.** Pictorial view of the Bernal spiral. Particles have been differently colored to highlight the presence of three strands. In this geometry, each particle has exactly six nearest neighbors.

two sets of simulations respectively as the temperature and polymer concentration routes, naming them after the respective relevant control parameters.

We study—as a function of the packing fraction and of the attraction strength—the shape of the clusters (quantified via their fractal dimension), the local geometry around each particle, the interparticle structure factor, and the connectivity properties of the system. We complement the static picture with information on the interparticle bond lifetime and on the dynamics of self-properties and collective properties. We compare these quantities for the two routes, and show that the two approaches provide a similar description of cluster growth, percolation, and gel formation.<sup>33</sup>

## II. Simulation Details

We study a system composed of  $N = 2500$  colloidal particles of diameter  $\sigma$  and mass  $m$  in a cubic box of size  $L$ , as a function of the packing fraction  $\phi_c = \pi\rho\sigma^3/6$ , where  $\rho = N/L^3$  is the number density, and of the temperature  $T$ . The particles interact simultaneously via a short-range potential  $V_{SR}$  and a screened electrostatic repulsive interaction  $V_Y$ . The short-range attraction is modeled for simplicity with the generalization to  $\alpha = 18$  of the Lennard-Jones  $2\alpha - \alpha$  potential, as proposed by Vliegthart et al.<sup>34</sup>

$$V_{SR}(r) = 4\epsilon \left[ \left( \frac{\sigma}{r} \right)^{2\alpha} - \left( \frac{\sigma}{r} \right)^\alpha \right] \quad (1)$$

where  $\epsilon$  is the depth of the potential. The parameters  $\sigma$  and  $\epsilon$  are chosen as units of length and energy, respectively. We also consider  $k_B = 1$ . For this choice of  $\alpha$  the width of the attraction range is roughly  $0.2\sigma$ . The phase diagram of  $V_{SR}(r)$  has been studied previously<sup>34</sup> and it is characterized by a rather flat gas–liquid coexistence line, with a critical point located at  $T_c^{SR} \approx 0.43$  and  $\phi_c^{SR} \approx 0.225$ .

The repulsive interaction is modeled by a Yukawa potential

$$V_Y(r) = A \frac{e^{-r/\xi}}{r/\xi} \quad (2)$$

characterized by an amplitude  $A$  and a screening length  $\xi$ . We focus on the case  $\xi = 0.5\sigma$  and  $A = 8\epsilon$ , for which the minimum of the pair potential  $V_{SR} + V_Y$  is located at  $r = 1.042\sigma$  corresponding to a potential energy  $E_{min} = -0.52\epsilon$ . With the present choice of  $A$  and  $\xi$ , the ground-state configuration of an isolated cluster is known to be the one-dimensional Bernal spiral, shown in Figure 1.<sup>20</sup> The Bernal spiral structure is composed of face-sharing tetrahedrons, resulting in three twisting strands of particles in such a way that each particle has six nearest neighbors. In this geometry, for large  $N$ , the potential energy per particle  $E$  is  $E = -1.36 + 2.10/N$  (always in units of  $\epsilon$ ). In the bulk of the spiral (far from side effects)  $E$  is about three times  $E_{min}$ , confirming that the attractive interaction with the six neighbors provides most of the binding energy.

In parallel, we also study the case in which the magnitude of the attractive part changes to mimic the dependence of the depletion interaction on polymer concentration  $\phi_p$ . As in ref 7,

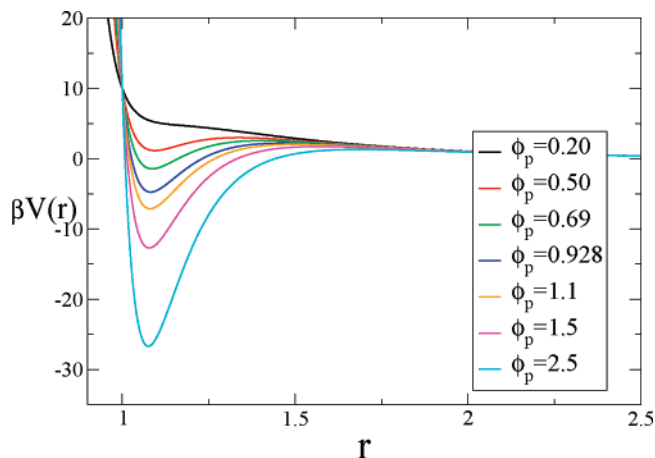


**Figure 2.** Interaction potential  $\beta V(r) \equiv \beta[V_{SR}(r) + V_Y(r)]$  for different values of the polymer concentration  $\phi_p$ . Here  $A = 10\epsilon$ ,  $\xi = 0.65\sigma$ ,  $\alpha = 10$ , and  $\beta\epsilon = 14.0\phi_p$ .<sup>7</sup>

we choose  $\epsilon/k_B T = 14\phi_p$ ; i.e., the attraction strength is assumed to depend linearly on the fraction of free volume occupied by polymers  $\phi_p$ . In this case, as in experiments,  $T$  is kept constant to  $k_B T = 1$ . To study a model as close as possible to the experimental work of ref 7, we select  $\xi = 0.65\sigma$ ,  $A = 10\epsilon$ ,<sup>35</sup> and  $\alpha = 10$ . For this value of  $\alpha$ ,  $r_{min} = 1.07\sigma$ , in agreement with the position of the maximum in the radial distribution function  $g(r)$ , as extracted from data reported in ref 7.

The dependence of the potential shape with  $\phi_p$  is shown in Figure 2. Note that  $V(r)$  changes from monotonically repulsive to repulsive with a *local* minimum (with  $V(r_{min}) > 0$ ). Finally, for  $\phi_p > 0.50$ ,  $V(r)$  develops an attractive global minimum followed by a repulsive tail.

In the rest of the present work, we will name  $T$ -route and  $\phi_p$ -route the two parallel sets of simulations. The short-range nature of  $V_{SR}$  favors a very effective way to define pairs of bonded particles. Indeed, the resulting potential  $V(r) = V_{SR} + V_Y$  has a well-defined maximum located approximately where the short-range attraction becomes negligible. In the following we will consider bonded (or nearest neighbors) all pairs of particles whose relative distance  $d < r_{max}$ . In the  $T$ -route case, we fix  $r_{max} = 1.28\sigma$ , the location of the local maximum in  $V_{SR} + V_Y$ . In the  $\phi_p$ -case the maximum exists only for  $\phi_p \geq 0.5$  and its location depends on the value of  $\phi_p$ , changing approximately between  $1.3\sigma$  and  $1.5\sigma$  in the investigated range, as shown in Figure 2. For convenience, in the  $\phi_p$ -route we choose  $r_{max} = 1.4\sigma$  which provides a good estimate of the bonding distance in the interesting cases of large  $\phi_p$  values. Note that in the manuscript we limit ourselves to the case  $\phi_p > 0.5$ , for which a well-defined minimum in  $V_{SR} + V_Y$  is present.

In all simulations, time is measured in units of  $\sqrt{m\sigma^2/\epsilon}$ . For numerical reasons, the repulsive potential is cut at  $r_c = 8\xi$ , such that  $V_Y(r_c) \approx 4.2 \times 10^{-3}A$ . All simulated state points are shown in Figure 3. In the  $T$ -route, a clear connection can be made with the thermodynamic behavior of the  $V_{SR}$  potential. All studied state points are located inside the spinodal region of the attractive potential. This is due to the fact that the spinodal is quite flat; see Figure 4B in ref 34. Equilibration is achieved with Newtonian dynamics, followed by a Brownian dynamics simulation, based on the scheme of ref 36, to produce equilibrium trajectories. In the case of Newtonian dynamics, the equation of motion have been integrated with a time step of  $\Delta t = 0.02$ . In the case of Brownian dynamics,  $\Delta t = 0.05$  with a bare diffusion coefficient  $D_o = 0.005$ . Equilibration runs required, at the slowest states, more than  $10^9$  integration time

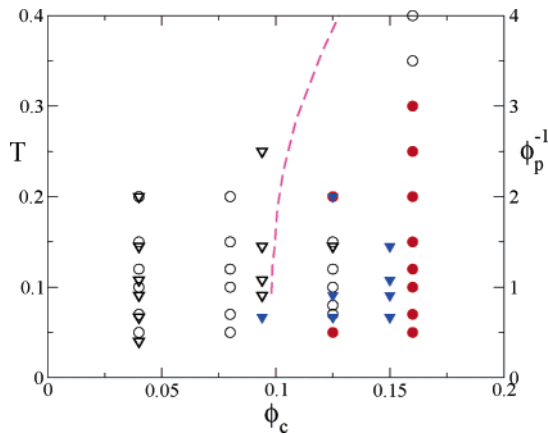


**Figure 3.** State points studied in this work, in the  $T - \phi_c$  (left y-axis) and  $\phi_p - \phi_c$  (right y-axis) planes, respectively, for the  $T$  (circles) and  $\phi_p$  (triangles) routes. Full symbols indicate state points where the equilibrium structure presents a spanning network of bonded particles. The dashed line represents the experimental percolation line of ref 7.

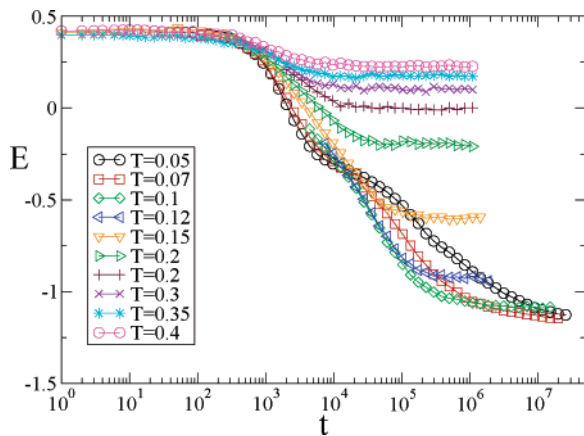


**Figure 4.** Time dependence of the potential energy following a quench starting from high temperature ( $T = 1.0$ ) for  $\phi_c = 0.16$ , for the  $T$ -route case.

steps, corresponding to about three months of computer time on a 1.6 GHz Pentium processor.

### III. Equilibration

Simulations are started from high  $T$  (or correspondingly  $\phi_p = 0$ ) equilibrium configurations and quenched to the selected final state. During equilibration, a Berendsen thermostat with a time constant of 10 is active, to dissipate the energy released in the clustering process. Following the quench, the time evolution of the potential energy  $E$  shows a significant drop. Equilibration becomes slower the lower the final  $T$  or the larger  $\phi_p$ . It also slows down on lowering the colloid packing fraction  $\phi_c$ . The evolution of  $E$  following a quench is shown in Figure 4 for the case  $\phi_c = 0.16$ . Around  $T \lesssim 0.07$ , equilibration cannot be achieved within the simulation time and dynamic arrest takes place. In these conditions, extremely slow (logarithmic in time) drift of  $E$  is still present at long times. To provide evidence that equilibrium is reached during the Newtonian simulation, we check that  $E$  is independent of the previous history and that clusters reversibly break and re-form on changing  $T$  or  $\phi_c$ . Similar results are obtained following the  $\phi_p$ -path.

The equilibration process is characterized by the progressive formation of bonds between particles and the corresponding growth of the particle's aggregates, the named clusters.

A quantification of the evolution of the structure of the system during equilibration can be provided by the structure factor  $S(q)$ ,

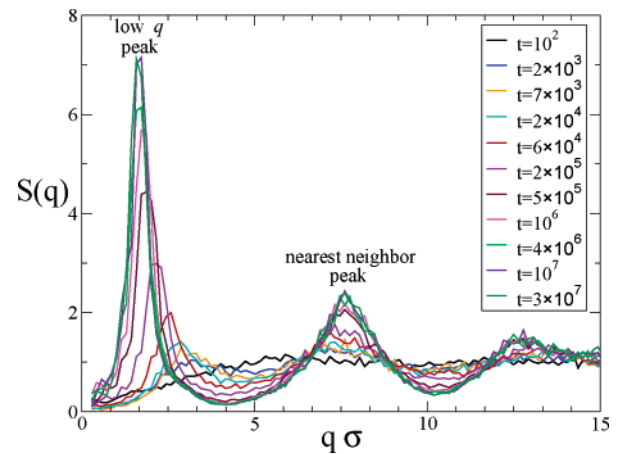


**Figure 5.** Evolution of the static structure factor  $S(q)$  during equilibration at  $\phi_c = 0.125$  and  $T = 0.08$ .

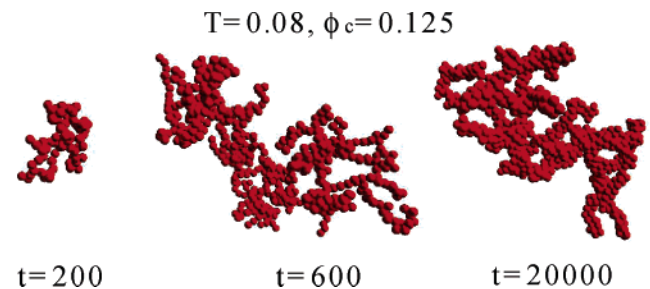


**Figure 6.** Snapshots of the largest cluster at three different times during the equilibration process. Here  $\phi_c = 0.125$  and  $T = 0.08$ . The cluster size is 72, 605, and 908, respectively at  $t = 200$ ,  $t = 600$ , and  $t = 20\,000$ .

defined as

$$S(q) = \left\langle \frac{1}{N} \sum_{ij} e^{-i\vec{q}(\vec{r}_i - \vec{r}_j)} \right\rangle \quad (3)$$

where  $\vec{r}_i$  indicates the coordinates of particle  $i$ . The  $S(q)$  evolution, shown in Figure 5, is reminiscent of the initial stages of spinodal decomposition, showing a low  $q$  peak which grows in amplitude and moves to smaller and smaller  $q$  vectors. While in spinodal decomposition, the coarsening process proceeds endless, in the present case the evolution of the small  $q$  peak stops when equilibrium is reached. The presence of the low  $q$ -peak in  $S(q)$ , at a finite wavevector, highlights the presence of an additional characteristic length scale in the system, discussed in more details in the next section.

Figure 6 shows the evolution of the shape of the largest cluster for the case  $\phi_c = 0.125$  and  $T = 0.08$ , one of the cases in which the average cluster size grows monotonically in time. It is interesting to observe that, at short times, the shape of the larger cluster is rather ramified, the potential energy is still large and locally the structure is still very different from the six-coordinated ground state structure. Cluster arms are essentially composed by particles arranged along lines. At longer times, the cluster arms get thicker and thicker, and the local configuration approaches the characteristic one of the Bernal spiral, even if some parts of the original branching points persist in the final structure favoring the formation of a gel network. The evolution of the shape, complemented with the time dependence of  $E$ , suggests that at large attraction strengths (low  $T$  or large  $\phi_p$ ), the equilibration process can be conceptually separated into two parts: an initial relaxation which is closely reminiscent of the one which would take place if the potential was purely

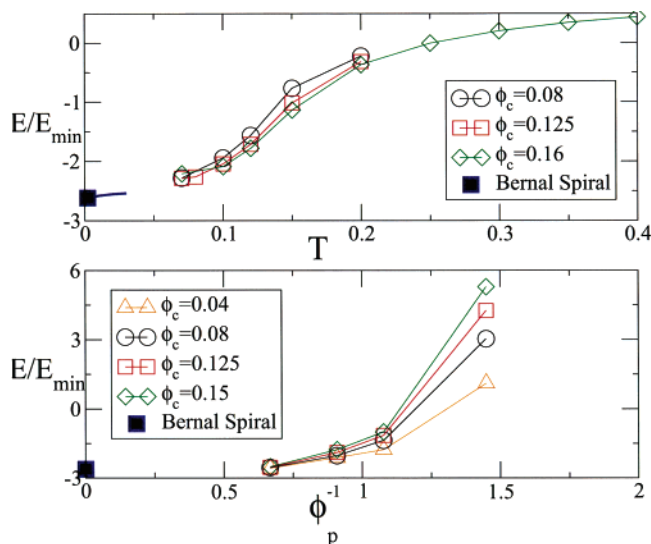


**Figure 7.**  $T$  (upper panel) and  $\phi_p$  (lower panel) dependence of the normalized potential energy per particle  $E/E_{\min}$  at different  $\phi_c$  values.  $E_{\min} = -0.52\epsilon$  in the  $T$ -route case, while it depends on  $\phi_p$  as  $E_{\min} = -14\phi_p kT + V_Y(r_{\min})$ , with  $r_{\min} = 1.07$ , in the  $\phi_p$  case. The corresponding value for the Bernal spiral configuration is also reported.

attractive, followed by a second rearrangement which sets in only after the coordination number has become significant. At this point, the competition of the long-range repulsion enters into play, forcing thereby the system to rearrange into the expected local configuration. This competition results also in a nonmonotonic evolution, during the equilibration, of the mean cluster size, at some state points.

#### IV. Equilibrium Properties: Statics

**A. Potential Energy.** The upper panel of Figure 7 shows the  $T$  dependence of  $E/E_{\min}$  at the studied values of  $\phi_c$ . Around  $T \approx 0.2$ ,  $E$  becomes negative, suggesting that the short-range attractive interaction becomes relevant. For lower  $T$ ,  $0.1 < T < 0.2$ ,  $E$  drops significantly, quickly reaching below  $T = 0.1$  a value compatible with the ground state Bernal spiral configuration (also shown), once the vibrational components are properly accounted for. A similar behavior is observed for the  $\phi_p$  dependence, shown in the lower panel of Figure 7. In the studied  $\phi_c$  range, the  $\phi_c$  dependence of  $E$  is rather weak, especially for large attraction strengths.

**B. Cluster Size Distribution.** In this section, we examine the cluster size distribution, as it evolves with  $\phi_c$  and  $T$ . Standard algorithms are used to partition particles into clusters of size  $s$  and to evaluate the cluster size distribution  $n_s$  and its moments. The first moment of the cluster size distribution

$$\langle s \rangle = \frac{\sum_s s n_s}{\sum_s n_s} = N/N_s \quad (4)$$

is connected to the inverse of the number of clusters  $N_s$ , while the second moment  $\langle s^2 \rangle$  provides a representative measure of the average cluster size

$$\langle s^2 \rangle \equiv \frac{\sum_s s^2 n_s}{\sum_s s n_s} \quad (5)$$

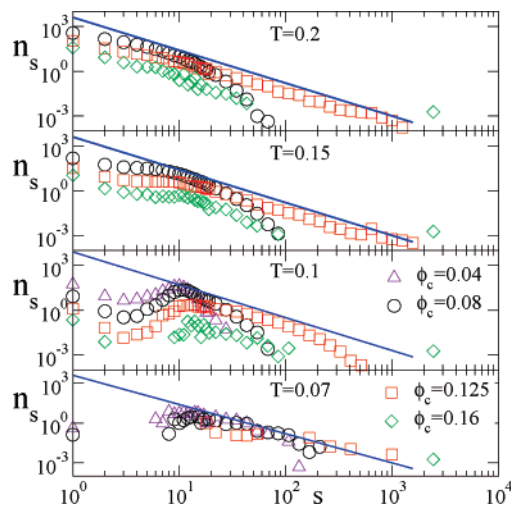


**Figure 8.** Cluster size distribution  $n_s$  at several  $T$ . In each panel, the full line represents the function  $n_s \sim s^{-2.2}$ .

We also examine the connectivity properties of the equilibrium configurations. Configurations are considered percolating when, accounting for periodic boundary conditions, an infinite cluster is present. To test for percolation, the simulation box is duplicated in all directions, and the ability of the largest cluster to span the replicated system is controlled. If the cluster in the simulation box does not connect with its copy in the duplicated system, then the configuration is assumed to be nonpercolating. The boundary between a percolating and a nonpercolating state point has been defined by the probability of observing infinite clusters in 50% of the configurations. To provide an estimate of the percolation locus, we report in Figure 3 the state points which are percolating. We note that, at this level, percolation is a geometric measure, and it does not provide any information on the lifetime of the percolating cluster. Indeed, at  $\phi_c = 0.125$ , percolation is present both at high  $T$ , where we observe geometric percolation of clusters with bonds of very short lifetime, and at low  $T$ , where the particles are connected by energetic bonds of very long lifetime, as discussed below. The competition between geometric and energetic percolation results in a intermediate temperature window where the system does not percolate, i.e., in a re-entrant percolation locus. A substantial agreement between the percolating states found here and those examined in ref 7 by confocal microscopy (see dashed line in Figure 3) is reported, except for the evidence of re-entrant percolation, which is missing in the experiment. This could be explained by a less transient bond formation in the real system with respect to the simulated model.

The cluster size distribution  $n(s)$  is shown in Figure 8. At  $T = 0.2$  (where  $E \approx 0$  and hence no significant bonding exists) upon increasing  $\phi_c$ , the distribution progressively develops a power-law dependence with an exponent  $\tau$ , consistent with the random percolation value  $\tau \approx -2.2$ .<sup>37,38</sup> Percolation is reached when  $0.125 < \phi < 0.16$ . At slightly lower  $T$ , i.e.,  $T = 0.15$ , the picture remains qualitatively similar, except for a hint of nonmonotonic behavior, around  $s \approx 10-20$ . On further lowering  $T$ , the number of clusters of size  $s \lesssim 10$  drops significantly, to eventually disappear at  $T = 0.07$ . These results are observed at all studied densities.

To frame the results presented above, we recall information previously obtained in the study of the ground-state energy of isolated cluster of different size.<sup>20</sup> For a cluster size  $s \lesssim 10$ , the addition of a monomer to an existing cluster lowers the energy per particle, since the gain associated with the formation of an additional attractive short-range bond is not yet compensated

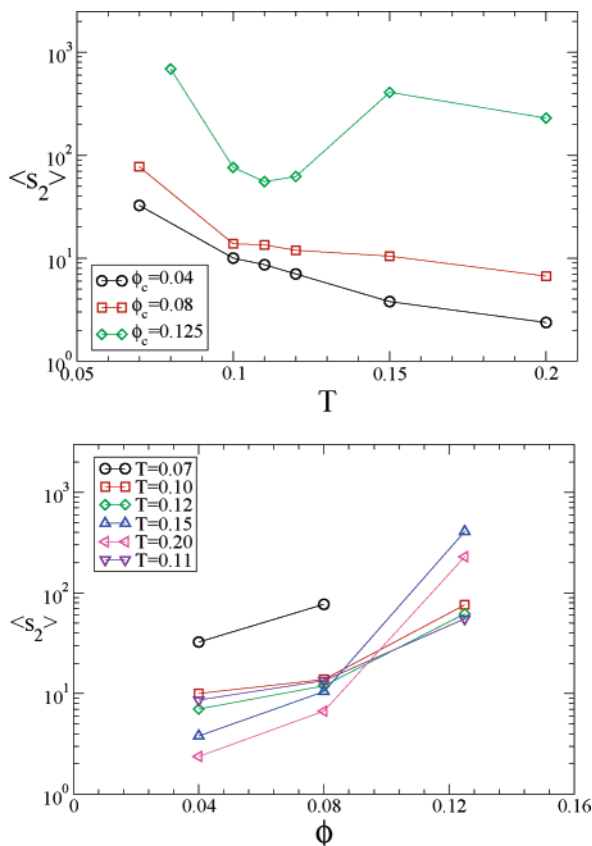


**Figure 9.** Temperature and  $\phi_c$  dependence of the second moment of the cluster size distribution  $\langle s_2 \rangle$ , for the  $T$ -route case.

by the increased number of repulsive interactions. However, when clusters have grown sufficiently, for  $s \gtrsim 10 - 20$ , the energy driving force for growing is reduced, since the energy per particle does not significantly depend any longer on the cluster size.<sup>20</sup> Isolated clusters results carry on to the interacting clusters case since the relatively small screening length does not produce a significant cluster–cluster interaction. Indeed, the effective cluster–cluster potential will be characterized, to a first approximation, by the same  $\xi$ ,<sup>16</sup> which is short as compared to the distance between clusters.

The high  $T$  percolation phenomenon observed at  $\phi_c = 0.125$  is not related to the establishment of long lifetime bonding between particles. Indeed, with the same definition of bond distance ( $1.28\sigma$ ), the hard-sphere fluid would be characterized by an infinite cluster already at  $\phi_c = 0.16$ . Hence, the high  $T$  percolation is only weakly controlled by the interparticle potential. Thus, it is not a surprise that, close to percolation, at high  $T$ ,  $n(s) \sim s^{-\tau}$  with  $\tau$  consistent with the random percolation value.<sup>37,38</sup> The disappearance of clusters of size  $s \lesssim 10$ , which starts to be visible for  $T \leq 0.1$ , signals the progressive role of energy in controlling clustering. At the lowest investigated  $T$ , energy has taken over and all clusters are formed by energetically convenient configurations. In this respect, we can think of the low  $T$  system as a fluid composed of super-aggregates, providing an effective renormalization of the concept of “monomer” in the fluid. The small cluster–cluster interaction energy may favor a reestablishment of the random percolation geometries and characteristic exponents, as discussed in the following.

Figure 9 shows the  $T$  and  $\phi_c$  dependence of the second moment of the distribution, the average cluster size  $\langle s_2 \rangle$ , defined in eq 5, for all nonpercolating state points. Apart from  $\phi = 0.16$ , where configurations are percolating already before

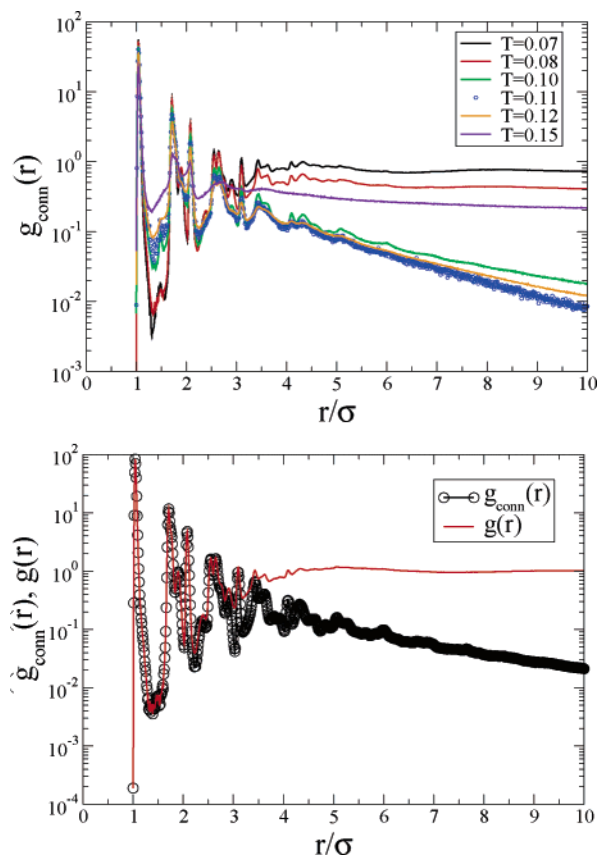


**Figure 10.** Top:  $g_{conn}(r)$  at  $\phi_c = 0.125$  for various temperatures. Bottom: Comparison of  $g_{conn}(r)$  and  $g(r)$  for the same state point  $\phi_c = 0.08$  and  $T = 0.07$ .

the physics of the short-range bonding sets in, percolation at small packing fractions is not reached at all temperatures we are able to equilibrate. At  $\phi_c = 0.125$ , a nonmonotonic dependence of  $\langle s_2 \rangle$  ( $T$ ) is observed, which we interpret as a crossover from the “random” percolation observed at high  $T$  to the bond-driven percolation, which becomes dominant at low  $T$ . The  $\phi_c$  dependence of  $\langle s_2 \rangle$  is shown in the bottom panel. At all  $T$ , a monotonic growth is observed.

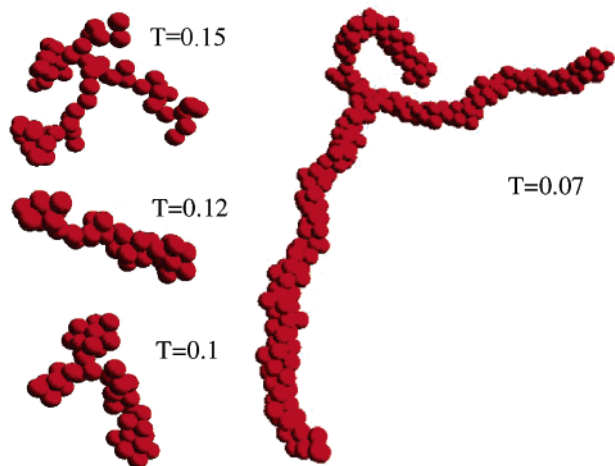
**C. Pair Connectedness Function.** Another useful metric of a cluster distribution is the pair connectedness function  $g_{conn}(r)$ , (also reported as  $P(r)$ ), defined as conditional probability of finding a particle at a distance  $r$  from a particle located at the origin, connected via a sequence of bonds, i.e., within the same cluster. The quantity  $g_{conn}(r)$  is used in classical percolation theory and can be determined by generalized integral equation,<sup>39–42</sup> leading to well-defined cluster sizes and statistics. Indeed, the average cluster size  $\langle s_2 \rangle$  is related to  $g_{conn}(r)$  as<sup>39</sup>

$$s_2 = 1 + \rho \int dr^3 g_{conn}(r) \quad (6)$$

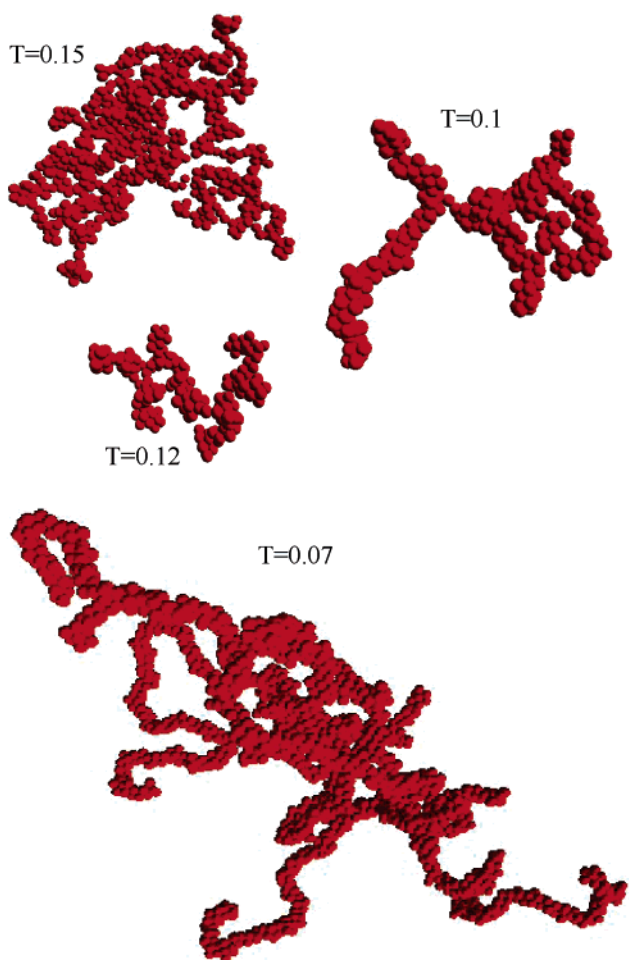
When an infinite cluster appears, the large  $r$  limit of  $g_{conn}(r)$  is different from zero.

Figure 10 (top) shows  $g_{conn}(r)$  along the  $\phi_c = 0.125$  isochore. In agreement with previous comments, the large distance limit of  $g_{conn}(r)$  indicates a reentrant behavior. Indeed, both at high  $T$  and at low  $T$ ,  $g_{conn}(r)$  is different from zero at large distances, while it reaches a zero value at intermediate  $T$  (e.g.,  $T = 0.11$ ). Significantly less structured peaks, for next and higher order neighbors, are observed at high  $T$  with respect to low  $T$ .

Figure 10 (bottom) compares, for one specific state point,  $g(r)$  and  $g_{conn}(r)$ . It is interesting to note that the oscillations in



**Figure 11.** Typical largest cluster at  $\phi_c = 0.08$  for four different  $T$  values: from top left to bottom right,  $T = 0.15, 0.12, 0.1,$  and  $0.07$ .



**Figure 12.** Same as Figure 11 for  $\phi_c = 0.125$ .

$g(r)$ , describing the liquid structure, are essentially retained into the  $g_{\text{com}}(r)$ , suggesting the intercluster interactions are negligible.

**D. Cluster Shape.** A pictorial description of the shape of the larger cluster observed in a typical configuration at  $\phi_c = 0.08$  and  $\phi_c = 0.125$  for different  $T$  is shown in Figures 11 and 12. In both cases, a progressive change of shape of the largest cluster is observed on cooling. A close look to the figures shows that on cooling particles become locally tetrahedrally coordinated and that the loose high  $T$  bonding progressively crosses to a one-dimensional arrangement of tetrahedrons. At the lowest  $T$ , the clusters are composed by large segments of

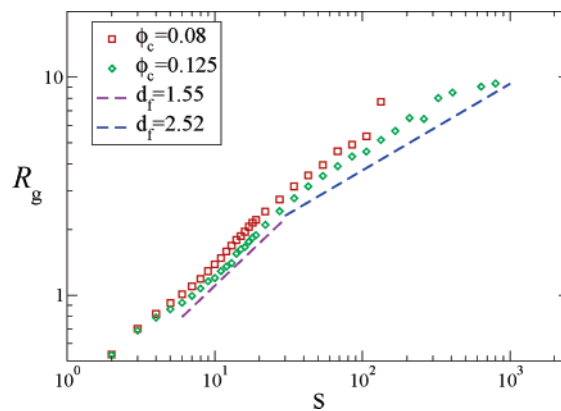


**Figure 13.** Size dependence of the cluster gyration radius at  $T = 0.15$  for two values of  $\phi_c$ . The dashed line provides a reference slope for the random percolation  $d_f$  value.

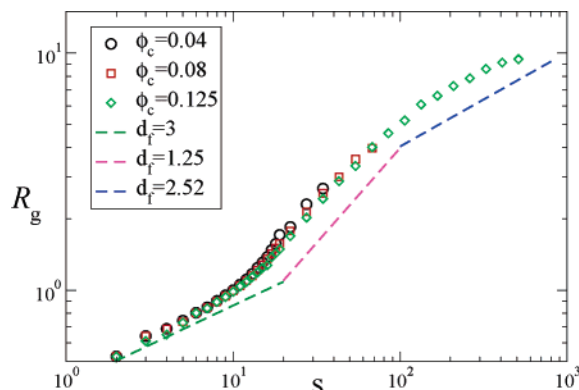


**Figure 14.** Size dependence of the cluster gyration radius at  $T = 0.1$  and several  $\phi_c$ . Lines provide reference slopes for different  $d_f$  values.

Bernal spiral structures joined in branching points, the latter providing the mechanism for network formation.

To quantify the cluster shape we study the cluster size dependence of the cluster radius of gyration  $R_g$ , defined as

$$R_g = \left[ \frac{1}{N} \sum_{i=1}^N (\mathbf{r}_i - \mathbf{R}_{CM})^2 \right]^{1/2} \quad (7)$$

where  $\mathbf{R}_{CM}$  are the cluster center of mass coordinates. For fractal aggregates,  $R_g \sim s^{1/d_f}$ , where  $d_f$  indicates the fractal dimension. The observed behavior of the clusters shape is very different at high and low  $T$ . Figure 13 shows  $R_g$  vs  $s$  for two representative state points at  $T = 0.15$ , close to percolation. The typical shape of the cluster at these two state points is reported in Figures 11 and 12. Of course, the bond lifetime (as discussed in the following) increases on cooling, and only at low  $T$  do clusters survive as well-defined entities for appreciable times. Hence at high  $T$ , clusters should be considered as simply transient arrangements of particles. In this respect, it is not a surprise that, when the cluster size is greater than 20 monomers, the fractal dimension is consistent with the random percolation value in three dimensions ( $d_f = 2.52$ ).<sup>37,38</sup> This value confirms that at high  $T$ , as discussed previously, the energetic of the bonds is negligible as compared to entropic effects and the cluster size grows on increasing  $\phi_c$ , mostly due to the increase in the average number of particles with a relative distance less than  $r_{\text{max}}$ . At low  $T$ , an interesting phenomenon occurs, shown in Figure 14. The very small clusters ( $s < 10$ ) are rather compact and  $d_f \approx 3$ , and indeed, in this size interval, the energy per particle in the cluster decreases on increasing cluster size.<sup>20</sup> For clusters with intermediate size  $10 \lesssim s \lesssim 100$ ,  $d_f \approx 1.25$ , supporting the

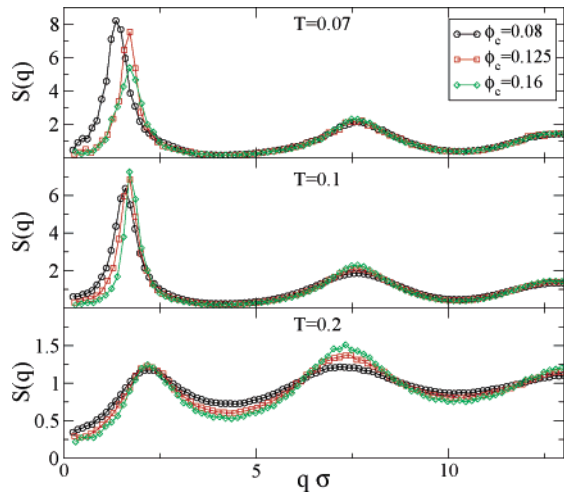


**Figure 15.** Wavevector  $q$  dependence of  $S(q)$  at three different  $T$  ( $T = 0.07, 0.1, 0.2$ ) for the  $T$ -route case. For each  $T$ , data at three  $\phi_c$  are reported ( $\phi_c = 0.08, 0.125, 0.16$ ).

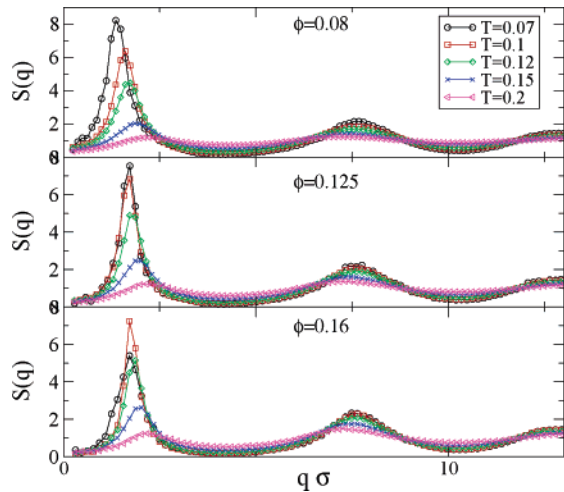


**Figure 16.** Wavevector  $q$  dependence of  $S(q)$  at three different  $\phi_c$  ( $\phi_c = 0.08, 0.125, 0.16$ ) for the  $T$ -route case. For each  $\phi_c$  data at several  $T$  are reported.

preferential one-dimensional nature of the elementary aggregation process, driven by the repulsive part of the potential. This  $d_f$  value is observed for all equilibrium cluster phases in which clusters of size  $10 < s < 100$  are dominant, with a small trend toward smaller values for smaller  $T$  and  $\phi_c$ . This small  $d_f$  value provides further evidence that in this size interval growth is essentially uniaxial, and that clusters of size 100 or less are essentially composed by pieces of Bernal spirals joined by few branching points<sup>20</sup> (see Figures 11 and 12). For larger  $s$  values, a crossover toward  $d_f \approx 2.52$  is observed. This crossover suggests that for larger clusters the one-dimensional bundles have branched a significant number of times, generating clusters whose geometry is again controlled by random percolation features. Pieces of Bernal spirals act as building blocks connected at branching points in a random fashion.

**E. Structure Factor.** As discussed in section III, the clustering process and the residual repulsive interactions between different clusters produce an additional low  $q$  peak in  $S(q)$ , located well below the location of the nearest neighbor peak ( $q\sigma \approx 2\pi$ ). Figures 15 and 16 show, respectively, the  $T$  and  $\phi_c$  dependence of  $S(q)$ , in equilibrium. Data refer to both percolating and nonpercolating state points. We observe no dependence of the position (either with  $T$  or  $\phi_c$ ) of the nearest-neighbor peak, consistent with the presence of a deep minimum in the

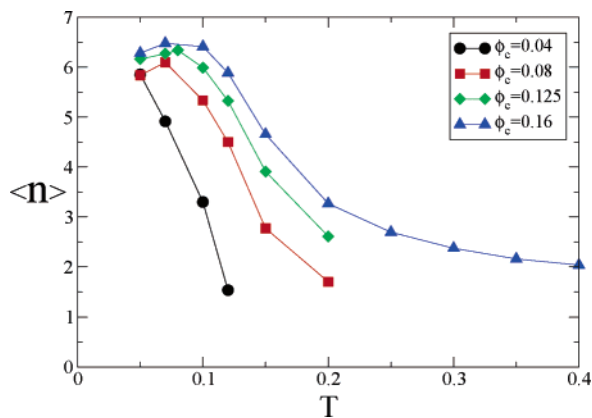
interaction potential, which defines quite sharply the interparticle distance. The amplitude of the nearest-neighbor peak grows on decreasing  $T$  or increasing  $\phi_c$ . The location of the cluster–cluster peak shows a weak  $\phi_c$  dependence, almost absent at  $T = 0.2$  (and higher  $T$ ), but which becomes more relevant at very low  $T$ . We note that, on isothermally increasing  $\phi_c$ , the location of the peak does not change even when percolation is crossed. On the other hand, the  $T$  dependence is significant and the location of the peak moves to smaller  $q$  on decreasing  $T$ , suggesting the establishment of longer correlation lengths. The  $T$  and  $\phi_c$  trends are quite similar to those recently observed in concentrated protein solutions at low ionic strength.<sup>4</sup> In particular, in that paper, the independence of the cluster peak position on  $\phi_c$  was interpreted as evidence of a linear dependence of the equilibrium cluster size with  $\phi_c$ . Indeed, if clusters are assumed to be rather monodisperse in size and if the inverse of the peak position is assumed to be a measure of the intercluster distance, the number cluster density has also to be independent of  $\phi_c$ .<sup>4</sup> It is worth stressing that, in one of the first papers addressing the possibility of equilibrium cluster phases in colloidal systems,<sup>13,43</sup> the same relation between equilibrium cluster size and  $\phi_c$  was presented, although its validity was limited to the case of clusters of size significantly larger than the one observed experimentally in ref 4, hinting to a wider validity of the relation suggested in ref 4. Here we note that the independence of the  $S(q)$  cluster peak position with  $\phi_c$  holds from very small  $\phi_c$  up to values well beyond percolation, where an interpretation in terms of finite clusters relative distance is clearly not valid. In the present study (of non spherical clusters), we can access both  $S(q)$  and the cluster size distribution. We note that, as shown in Figure 8, the cluster size distribution does not peak around a typical value. Actually, the cluster size is significantly nonmonodisperse, especially close to percolation. We also note that neither  $\langle s_1 \rangle$  nor  $\langle s_2 \rangle$  (see Figure 9) scale linearly with  $\phi_c$ , despite the constant position of the low  $q$  peak in  $S(q)$ .

It would be relevant to understand how the parameters  $A$  and  $\xi$  entering the potential (see eqs 1 and 2) control the position of the cluster peak and its  $T$  and  $\phi_c$  dependence. In the case of spherical clusters, it was possible to associate the peak position to the average distance between clusters, since no percolation was observed. This explanation is not fully satisfactory for the present model, since, as can be seen in Figure 16 for the case of  $T = 0.2$ , the location of the peak is clearly the same both in the nonpercolating state  $\phi = 0.125$  and in the percolating state  $\phi = 0.16$ . A better understanding of the quantities controlling the peak position is requested. A first attempt in this direction has been recently presented.<sup>15</sup>

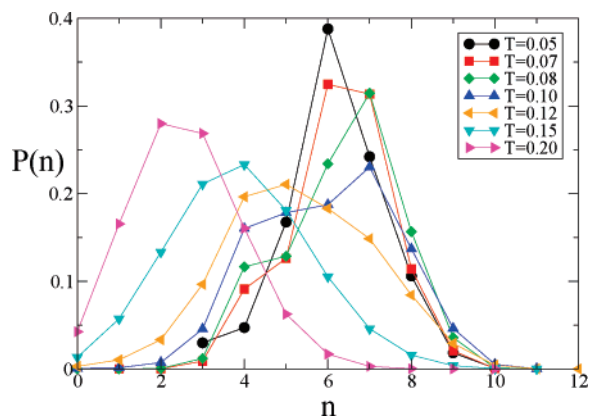
**F. Local Order.** A simple and useful indicator of local order is provided by the average number of nearest neighbors  $\langle n \rangle$  and by the associated distribution of nearest neighbors  $P(n)$ , which counts the fraction of particles surrounded by  $n$  neighbors within  $r_{max}$ . As shown in Figure 17,  $\langle n \rangle$  grows upon progressively lowering  $T$ , approaching, in a nonmonotonic way, a coordination number of 6.

Figure 18 shows the  $T$  evolution of the distribution  $P(n)$ . Again, a clear preference for local geometries with about six neighbors is displayed at low  $T$  a condition which is hardly observed in other materials in which particle–particle interaction is spherically symmetric. The value  $\langle n \rangle = 6$  is consistent with a local geometry of face-sharing tetrahedra.

Another useful indicator of local order, which enables us to effectively quantify the local structure, is provided by the so-called local orientation order parameters  $\bar{q}_{lm}(i)$  defined as



**Figure 17.** Average number of neighbors  $\langle n \rangle$  as a function of  $T$  for different  $\phi_c$  values. Note that, for all  $\phi_c$ , all curves approach the  $\langle n \rangle = 6$  value characteristic of the geometry of the Bernal spiral.



**Figure 18.** Distribution of the number of neighbors  $P(n)$  for several  $T$  at  $\phi_c = 0.125$  (for the  $T$ -route case).

$$\bar{q}_{lm}(i) \equiv \frac{1}{N_{b_i}} \sum_{j=1}^{N_{b_i}} Y_{lm}(\hat{r}_{ij}) \quad (8)$$

where  $N_{b_i}$  is the set of bonded neighbors of a particle  $i$ . The unit vector  $\hat{r}_{ij}$  specifies the orientation of the bond between particles  $i$  and  $j$ . In a given coordinate frame, the orientation of the unit vector  $\hat{r}_{ij}$  uniquely determines the polar and azimuthal angles  $\theta_{ij}$  and  $\phi_{ij}$ . The  $Y_{lm}(\theta_{ij}, \phi_{ij}) \equiv Y_{lm}(\hat{r}_{ij})$  are the corresponding spherical harmonics. Rotationally invariant local properties can be constructed by appropriate combinations of the  $\bar{q}_{lm}(i)$ . In particular, local order in crystalline solids, liquids, and colloidal gels, has been quantified, focusing on

$$q_l(i) \equiv \left[ \frac{4\pi}{2l+1} \sum_{m=-l}^l |\bar{q}_{lm}(i)|^2 \right]^{1/2} \quad (9)$$

and

$$\hat{w}_l(i) \equiv w_l(i) \left[ \sum_{m=-l}^l |\bar{q}_{lm}(i)|^2 \right]^{3/2} \quad (10)$$

with

$$w_l(i) \equiv \sum_{\substack{m_1, m_2, m_3 \\ m_1 + m_2 + m_3 = 0}} \begin{pmatrix} l & l & l \\ m_1 & m_2 & m_3 \end{pmatrix} \bar{q}_{lm_1}(i) \bar{q}_{lm_2}(i) \bar{q}_{lm_3}(i) \quad (11)$$

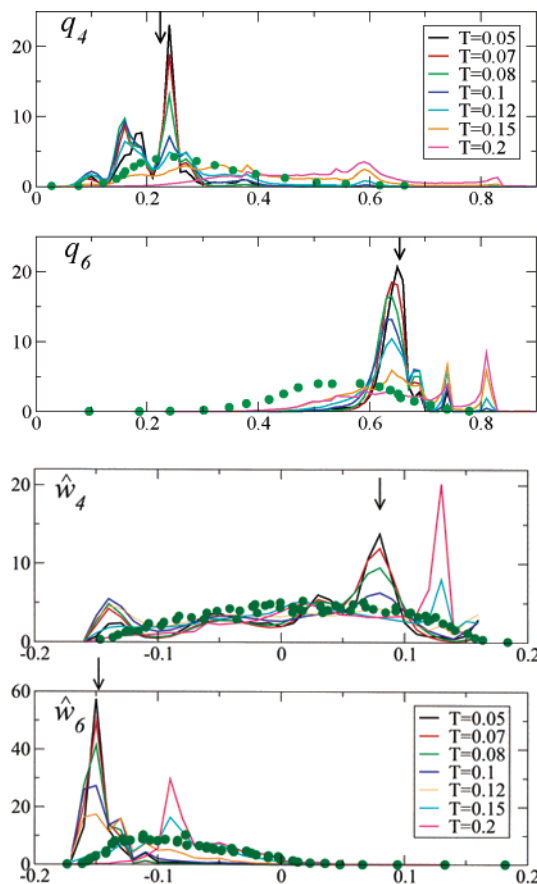


**Figure 19.** Temperature dependence of the rotational invariant distributions  $P(q_l)$  (top) and  $P(\hat{w}_l)$  (bottom) for  $l = 4$  and  $l = 6$  at  $\phi = 0.125$ . Arrows indicate the ideal Bernal spiral values. In the ideal spiral, the local surrounding of all particles is identical and hence the rotational invariant distributions are  $\delta$  functions. Filled circles are experimental data from ref 7.

The distributions of the  $q_l$  and  $\hat{w}_l$  parameters provide a sensitive measure of the local environment and bond organization. For example, dimers are characterized by  $q_1 = 1$ ,  $\hat{w}_4 = 0.13$  and  $\hat{w}_6 = -0.09$ . A local tetrahedral order is characterized by large negative values of  $\hat{w}_6$ , up to the value  $-0.17$  for the icosahedron.<sup>44</sup> For the perfect Bernal spiral of Figure 1, the orientational order parameters are determined as  $q_4 = 0.224$ ,  $q_6 = 0.654$ ,  $\hat{w}_4 = 0.08$ , and  $\hat{w}_6 = -0.148$ . Figure 19 shows the  $q_4$ ,  $q_6$ ,  $\hat{w}_4$ , and  $\hat{w}_6$  distributions and how they evolve with decreasing temperature for  $\phi = 0.125$ . We note that, upon cooling, the progressive presence of dimers and small clusters disappears and the distributions evolve toward a limiting form which appears to be specific of the Bernal spiral type of cluster. At low  $T$ , and in particular below  $T = 0.1$ , all distributions peak close to the characteristic values of the Bernal spiral. The local orientation order parameters have been evaluated in the confocal experimental work of ref 7, and they are represented in Figure 19 as filled symbols. There, it was shown that the experimental data are consistent with the Bernal geometry. In the analysis of the experimental data, the position of the particles in the perfect spiral geometry was subjected to some random displacements, to account for thermal fluctuations, possible intrinsic errors in the localization of the particles, and polydispersity in size (and/or charge) in the samples. After this procedure, the sharp peaks displayed in Figures 19 and 20 disappear, and smooth distributions are obtained, which compare well with the experimental data.

Figure 20 shows that, at low  $T$ , the distributions appear to be insensitive to  $\phi_c$ , in agreement with observations in ref 7 and

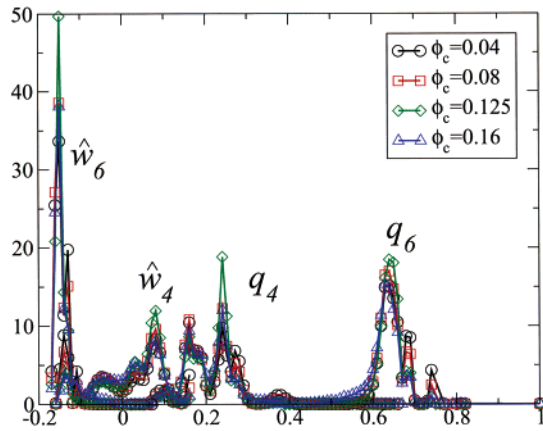


**Figure 20.** Packing fraction dependence of the rotational invariant distributions  $P(q_i)$  and  $P(w_i)$  for  $l = 4$  and  $l = 6$  at  $T = 0.07$ . Note that, at this low  $T$ , no  $\phi_c$  dependence is present.

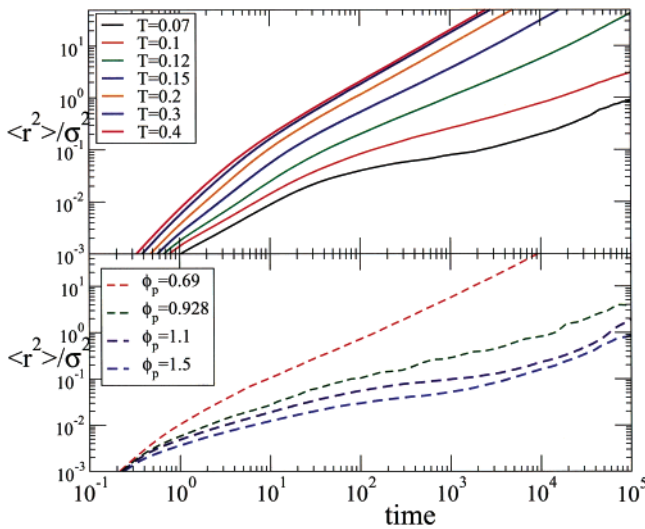


**Figure 21.** Averaged mean-square displacement  $\langle r^2 \rangle$  for the  $T$ -route (top) and the  $\phi_p$ -route (bottom) in log–log scale. In the top panel,  $\phi_c = 0.16$ , while in the bottom one,  $\phi_c = 0.15$ .

supporting once more that the local structure around the majority of the particles is similar to the ground-state structure provided by the Bernal spiral.

## V. Dynamics and Gel Formation

In this section, we present results for the particle dynamics as a function of  $\phi_c$  and  $T$  (in the  $T$ -route), or  $\phi_p$  (in the  $\phi_p$ -route). As for the equilibrium data shown in the previous section, dynamical quantities are evaluated from trajectories generated according to Brownian dynamics. The mean-square displacement,  $\langle r^2(t) \rangle$ , averaged over all particles and several starting times is shown in Figure 21 for one specific  $\phi_c$  value both for the  $T$  and the  $\phi_p$  routes.

Beyond the ballistic region (which extends up to  $\langle r^2(t) \rangle \lesssim 10^{-3}\sigma^2$ ), particles enter into a diffusive regime, composed of two different processes. A short transient where the bare self-diffusion coefficient  $D_o$ , set by the Brownian algorithm, dominates and a long-time region when particles feel the interparticle bonding. At high  $T$ , in the latter regime, particles diffuse almost freely, with a diffusion coefficient not very different from the bare self-diffusion  $D_o$  value. Upon cooling,  $\langle r^2(t) \rangle$  progressively develops a plateau, more evident for  $T \lesssim 0.1$ , which reaches the value  $\approx 4 \times 10^{-2}$ . If we look at the  $\phi_p$ -data, we observe a very similar behavior, with a very similar

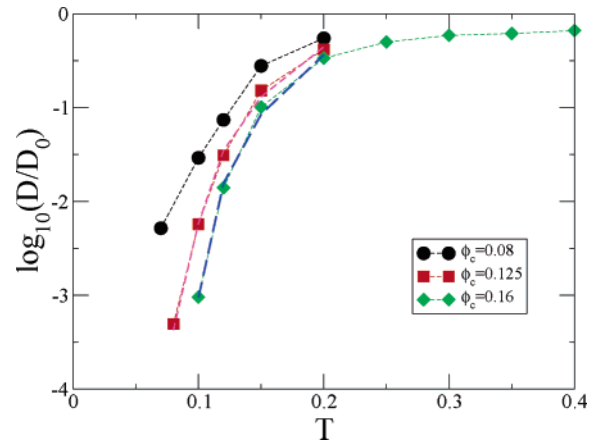


**Figure 22.** Temperature dependence of the normalized diffusion coefficient  $D/D_o$ , for different  $\phi_c$  values. The short and long dashed lines represent power law fits with exponent  $\gamma_D = 2.15$  and  $\gamma_D = 2.37$  and dynamic critical temperatures  $T_d = 0.084$  and  $T_d = 0.091$  respectively for  $\phi_c = 0.125$  and  $\phi_c = 0.16$ .

plateau which develops for  $\phi_p \gtrsim 0.9$ . These results signal that particles become tightly caged, with a localization length not very different from the one observed in the case of dynamic arrest in glass-forming systems, although in the present case caging is much less resolved. Increasing the attraction strength, the long time limit of  $\langle r^2(t) \rangle$  remains proportional to  $t$ , but with a smaller and smaller coefficient.

A global view of the  $T$  dependence of the slow dynamics is shown in Figure 22, where the long time limit of  $\langle r^2(t) \rangle/6t$ , i.e., the self-diffusion coefficient  $D$ , is reported. While at high  $T$  the diffusion coefficient approaches the bare self-diffusion coefficient, on cooling, in the same  $T$  interval in which a substantial bonding takes place,  $D$  drops several order of magnitudes, signaling a significant slowing down of the dynamics and the approach to a dynamically arrested state. The same behavior is observed for the  $\phi_p$  route, where  $D$  approaches a very small value for  $\phi_p \geq 1.1$ .

It is interesting to note that, for  $\phi_c = 0.125$  and  $\phi_c = 0.16$ , the  $T$  dependence of  $D$  is compatible with a power law, with exponent  $\gamma_D \approx 2.2$ , not very different from the typical values of  $\gamma_D$  predicted by mode coupling theory (MCT) for simple liquids. The case of  $\phi_c = 0.16$  is particularly interesting, since at all  $T$ , the instantaneous configuration of the system is percolating, providing a clear example of the difference between percolation and dynamic arrest. Vanishing of  $D$  is observed only at very low  $T$ , well below percolation. It is tempting to state that, when the cluster–cluster interaction is weak as in the present case, dynamic arrest always requires the establishment of a percolating network of attractive bonds, though this is not a sufficient condition since the bond lifetime should be significantly long. When repulsive cluster–cluster interactions are not negligible, arrest at low  $\phi_c$  can be generated in the absence of percolation<sup>16</sup> via a Yukawa glass mechanism.

Another important quantity to characterize dynamic arrest (particularly relevant for attraction-driven slowing down<sup>45</sup>), is the bond correlation function  $\phi_B(t)$ , defined as

$$\phi_B(t) = \left\langle \frac{\sum_{i < j} n_{ij}(t)n_{ij}(0)}{N_B(0)} \right\rangle \quad (12)$$

Here  $n_{ij}(t)$  is 1 if two particles are bonded and 0 otherwise, while  $N_B(0) \equiv \langle \sum_{i < j} n_{ij}(0) \rangle$  is the number of bonds at  $t = 0$ . The average is taken over several different starting times.  $\phi_B$  counts which fraction of bonds found at time  $t = 0$  is still present after time  $t$ , independent of any breaking–re-forming intermediate process.

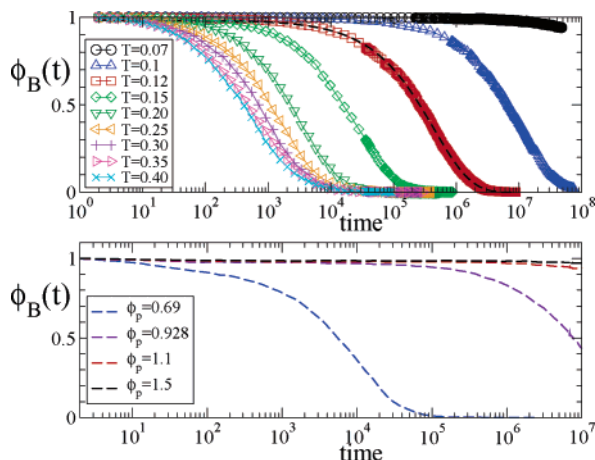


**Figure 23.** Bond correlation function  $\phi_B(t)$  for  $\phi_c = 0.16$  ( $T$ -route, top) and for  $\phi_c = 0.15$  ( $\phi_p$ -route, bottom). The  $\phi_B(t)$  shape can be well fitted by a stretched exponential function with stretching exponent  $\beta = 0.73$  (dashed line superimposed to the  $T = 0.12$  curve).

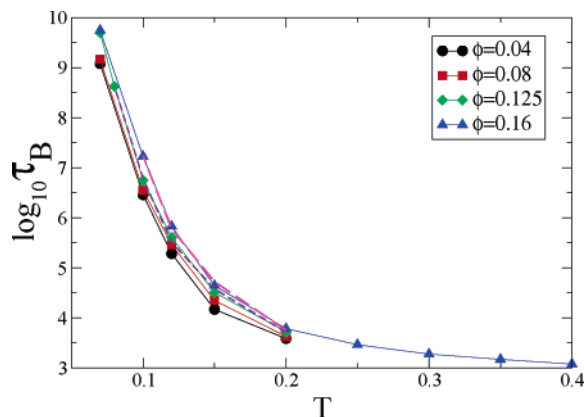


**Figure 24.** Temperature dependence of the bond lifetime  $\tau_B$  at all studied densities. The short and long dashed lines represent power law fits with exponent  $\gamma_\tau \approx 3.5$  and  $\gamma_\tau \approx 4.0$  and dynamic critical temperatures  $T_d = 0.084$  and  $T_d = 0.085$ , respectively, for  $\phi_c = 0.125$  and  $\phi_c = 0.16$ . The  $T = 0.07$  point, not included in the fits, is shown here only as an indication, since equilibrium is not properly reached at this  $T$ .

Figure 23 shows the evolution of  $\phi_B(t)$  with  $T$  and  $\phi_p$ . When dynamics slows down, the shape of  $\phi_B(t)$  is preserved at all  $T$  or  $\phi_p$ . The shape can be modeled with high accuracy with a stretched exponential function  $A \exp(-(t/\tau)^\beta)$ , with stretching exponent  $\beta \approx 0.73$ .

An estimate of the average bond lifetime  $\tau_B$  can be defined as  $\tau_B = \tau/\beta\Gamma(1/\beta)$ , where  $\tau$  and  $\beta$  are calculated via stretched exponential fits and  $\Gamma$  is the Euler  $\Gamma$  function.

Figure 24 shows  $\tau_B$  vs  $T$ . Analogous considerations to those reported above in discussing the  $T$  dependence of  $D$  apply. Indeed,  $\tau_B(T)$  is consistent with a power law with exponent  $\gamma_\tau$  varying between 3.5 and 4.0, larger than the one found for  $D(T)$ , but with consistent predictions for the diverging  $T$ .

We notice that, at  $T = 0.07$ , dynamics is extremely slow and bonds are almost unbroken in the time window explored in the simulation. It would be interesting to find out if the  $T$  dependence of  $\tau_B$  crosses to a different functional form at low  $T$  when all bonds are formed and if such crossover bears some analogies to the crossover from power-law to super Arrhenius observed in glass forming molecular systems. Unfortunately, as in the molecular glass cases, the time scale today available to simulation studies does not allow us to resolve this issue.

To further compare the arrest observed in the present system and the slowing down of the dynamics observed in other systems

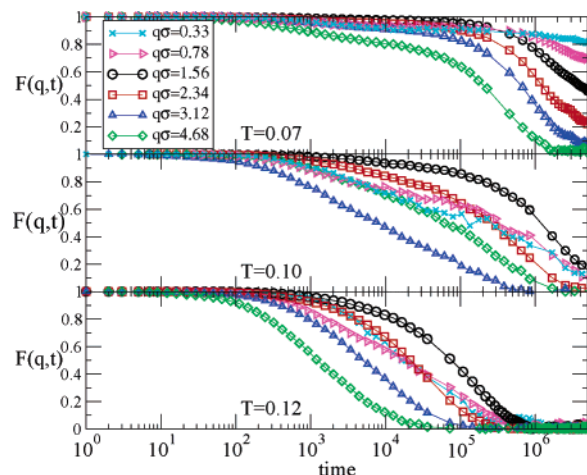


**Figure 25.** Wavevector  $q$  dependence of the intermediate scattering function  $F(q,t)$  at  $T = 0.07, 0.10, 0.12$  (from top to bottom) for  $\phi_c = 0.16$ . The reported  $q\sigma$  values are, respectively, 0.33, 0.78, 1.56, 2.34, 3.12, and 4.68.

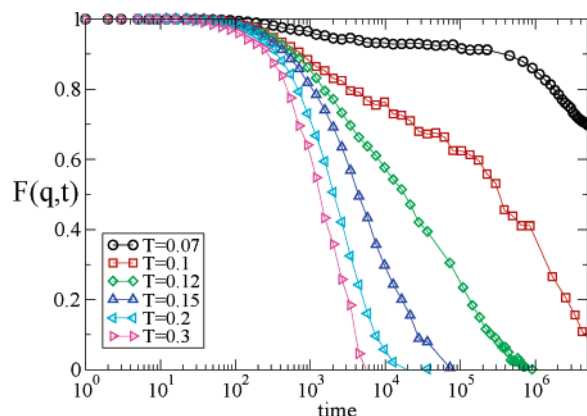


**Figure 26.** Temperature dependence of the intermediate scattering function  $F(q,t)$  at  $\phi_c = 0.16$  and  $q\sigma = 0.78$ . The reported  $T$  are 0.07, 0.1, 0.12, 0.15, 0.2, 0.25, 0.3, and 0.4.

close to dynamic arrest, we calculate the collective intermediate scattering function  $F(q,t)$ , defined as

$$F(\vec{q}, t) = \left\langle \frac{1}{N} \sum_{i,j} e^{-i\vec{q}(\vec{r}_i(t) - \vec{r}_j(0))} \right\rangle \quad (13)$$

where the average is calculated over different starting initial times. Figure 25 shows the  $q$  dependence of the  $F(q,t)$  at three different  $T$  values. The decay of the correlation functions does not show any appreciable intermediate plateau for any  $q$ . The functional form of the decay is strongly dependent on  $q$ , crossing from an almost  $\log(t)$  decay at small  $q$  to a less stretched decay at large  $q$  values. At the lowest  $T$  ( $T = 0.07$ ),  $F(q,t)$  does not decay to zero any longer, confirming that a nonergodic state has been reached. The nonergodic behavior manifests for very small values of  $q\sigma$ , in the range of the low  $q$  peak in  $S(q)$ , while ergodicity is restored at nearest neighbor length.<sup>46</sup> Figure 26 contrasts, at fixed  $q$  value, the  $T$  dependence of the dynamics. The shape of  $F(q,t)$  is sufficiently different to conclude that time-temperature superposition does not hold for this observable. We also note that at very low  $\phi_c$  ( $\phi_c = 0.04$  or  $0.08$ ) all density correlation functions decay to zero, within the explored time window, suggesting that cluster diffusion allows for the decay of density fluctuation, even in the presence of a nonergodic bond restructuring process. This suggests that, at low  $\phi_c$ , in the absence of percolation, density fluctuations are ergodic.

## VI. Conclusions

In this work we have presented a detailed analysis of the structural and dynamic properties of a colloidal dispersion in which the short-range attraction is complemented by a screened electrostatic repulsion. We have studied one specific choice of the parameters controlling the repulsive potential. In particular, we have chosen a screening length comparable to the radius of the colloidal particles. For this screening length, a study<sup>20</sup> of the ground-state structure of isolated clusters showed that the preferential local structure is composed by a one-dimensional sequence of face-shared tetrahedra, generating a local six-coordinated structure and a Bernal spiral shape.

The collective behavior of the system is very much influenced by the competition between attraction and repulsion, which in the present model sets in when  $T$  becomes smaller than 0.2 (in units of the depth of the attractive part). The relative location of the particles, which for  $T \gtrsim 0.2$  is mostly controlled by translational entropy, for  $T \lesssim 0.2$  depends more and more on energetic factors. Between  $T = 0.2$  and  $T = 0.1$ , the number of bonded pairs increases significantly, and the local structure evolves progressively toward the six-coordinated one characteristic of the Bernal spiral. At the lowest studied  $T$ ,  $T = 0.07$ , the cluster shape becomes independent of  $\phi_c$  and the ground-state local configuration becomes dominant. The cluster size distributions at low  $T$  show a very clear suppression of clusters of size  $\lesssim 10$ , the size requested for the establishment of a bulk component in the spiral configuration.

Although the majority of particles tends to preferentially sit in the 6-coordinated configuration, some particles are located in defective regions of the spiral, which act as branching points and favor the formation of large ramified fractal clusters, whose elementary units are spirals of finite size. It is interesting to investigate if the small energetic cost of branching allows us to model the spiral segments as renormalized monomers. In support of this possibility, we have detected a progressive increase of the cluster fractal dimension for cluster of size  $s \gtrsim 100$ . We have also shown that, consistent with the ground-state calculations, clusters of size  $s \lesssim 10$  are almost spherical, while clusters of size  $10 \lesssim s \lesssim 100$  are characterized by  $d_f \approx 1.25$ .

The one-dimensional growth followed by a dynamic arrest phenomenon, observed in this work is reminiscent of the aggregation process in several protein solution systems.<sup>47–50</sup> In this class of protein solutions, a variation in the external control parameters (temperature, ionic strength, pH) often trigger an aggregation process of proteins into cylindrical clusters which, by branching mechanisms, forms a macroscopic gel, similar to what takes place in the system here investigated. Results reported in this work confirm that, as speculated in ref 20, there is a range of small but finite temperatures in which branching of the one-dimensional structure is preferred to cluster breaking and that such branching does indeed help establishing a connected three-dimensional network.

It is important to stress that the dynamic arrest mechanism observed in this work is very different from the one observed numerically for the case of  $\xi \approx 1.2\sigma$ .<sup>16</sup> In that case, clusters grow mostly spherical and do not present branching points. The slowing down of the dynamics in the  $\xi \approx 1.2\sigma$  case arises from the residual repulsive cluster-cluster interaction, resulting in the formation of a cluster phase or a repulsive cluster glass, analogous to the mechanisms suggested for Wigner glass systems. Indeed, in the arrested state, no percolation was detected. The arrested state generated via a Wigner glass transition discussed in ref 16 and the one generated via branching of one-dimensional clusters discussed in this work,

although differing only by modest changes in the experimental conditions, are probably characterized by significantly different viscoelastic properties. Indeed we expect that the Wigner glass will be much weaker than the stiff percolating structure generated by a continuous sequence of particles tightly bounded to six neighbors.

The system studied in this work is a good candidate for a thorough comparison with the slowing down characteristic of glass forming materials. The numeric “exact” equilibrium particle structure factor could be used as input in the mode coupling theory, along the lines theoretically suggested in ref 14 to provide a full comparison of the theoretical predictions for the arrest line as well as for the shape of the correlation functions. It would be interesting to quantify the role of the cluster pre-peak in the structure factor in the predicted slowing down of the dynamics.

Results presented in this work also provide further example of the existence of equilibrium cluster phases, a phenomenon which is recently receiving a considerable interest. Cluster phases have recently been investigated in systems as different as protein solutions,<sup>4,5,12</sup> colloidal dispersions,<sup>1,4,7,10</sup> Laponite,<sup>51</sup> liposomic solutions,<sup>11,52–56</sup> star-polymers,<sup>8</sup> aqueous solutions of silver iodide,<sup>3</sup> and metal oxides<sup>6</sup> and in recent numerical studies.<sup>16–18,21</sup> In all cases, the combination of the repulsive interactions with the short-range attraction appears to be crucial in stabilizing the cluster phase. The high sensitivity of the cluster shape and the final topology of the arrested state on the detailed balance between range and amplitude of the attractive and repulsive part of the potential brought forward by this and previous studies add new challenges to the modern research in soft condensed matter and to the possible technological exploitations of these new materials.

A final remark concerns the use of an effective potential, with state-independent parameters for the description of systems in which the screening length can be a function of the colloid packing fraction and in which the significant changes in structure with  $T$  (or concentration of depletant) may lead to relevant changes in the cluster surface potential or in the spatial distribution of ions. The similarity between the numerical data reported in this manuscript and the closely related experimental results suggest that, despite the approximation adopted in the numerical work, the essence of the arrest phenomenon is captured by the present models.

**Acknowledgment.** We thank P. Bartlett and J. van Duijnvelde for sharing their results with us, for discussions and for calling our attention on the  $\hat{w}$  distributions. We acknowledge support from the MIUR-FIRB and the MCRN-CT-2003-504712.

## References and Notes

- (1) Segré, P. N.; Prasad, V.; Schofield, A. B.; Weitz, D. A. *Phys. Rev. Lett.* **2001**, *86*, 6042–6045.
- (2) Dinsmore, A. D.; Weitz, D. A. *J. Phys.: Condens. Matter* **2002**, *14*, 7581–7597.
- (3) Mladenovic, I.; Kegel, W.; Bomans, P.; Frederik, P. *J. Phys. Chem. B* **2003**, *107*, 5717.
- (4) Stradner, A.; Sedgwick, H.; Cardinaux, F.; Poon, W. C. K.; Egelhaaf, S. U.; Schurtenberger, P. *Nature* **2004**, *432*, 492–495.
- (5) Baglioni, P.; Fratini, E.; Lonetti, B.; Chen, S.-H. *J. Phys.: Condens. Matter* **2004**, *16*, S5003–S5022.
- (6) Validzic, I. L.; van Hooijdonk, G.; Oosterhout, S.; Kegel, W. *Langmuir* **2004**, *20*, 3435.
- (7) Campbell, A. I.; Anderson, V. J.; van Duijnvelde, J.; Bartlett, P. *Phys. Rev. Lett.* **2005**, *94*, 208301.
- (8) Stiakakis, E.; Petekidis, G.; Vlassopoulos, D.; Likos, C. N.; Iatrou, H.; Hadjichristidis, N.; Roovers, J. *Europhys. Lett.*, in press.
- (9) Sanchez, R.; Bartlett, P. *condmat/0506566*, 2005.

- (10) Sedgwick, H.; Egelhaaf, S. U.; Poon, W. C. K. *J. Phys.: Condens. Matter* **2004**, *16*, 4913–+.
- (11) Bordi, F.; Cametti, C.; Diociaiuti, M.; Sennato, S. *Phys. Rev. E* **2005**, *71*, 050401.
- (12) Sedgwick, H.; Kroy, K.; Salonen, A.; Robertson, M. B.; Egelhaaf, S. U.; Poon, W. C. K. *Eur. Phys. J. E* **2005**, *16*, 77–80.
- (13) Groenewold, J.; Kegel, W. K. *J. Phys. Chem. B* **2003**, *105*, 11702–11709.
- (14) Wu, J.; Liu, Y.; Chen, W.-R.; Cao, J.; Chen, S. *Phys. Rev. E* **2004**, *70*, 050401.
- (15) Liu, Y.; Chen, W.-R.; Chen, S. *J. Chem. Phys.* **2005**, *122*, 044507.
- (16) Sciortino, F.; Mossa, S.; Zaccarelli, E.; Tartaglia, P. *Phys. Rev. Lett.* **2004**, *93*, 055701.
- (17) Sator, N.; Fierro, A.; Del Gado, E.; Coniglio, A. *condmat/0312591*, 2003.
- (18) Coniglio, A.; De Arcangelis, L.; Del Gado, E.; Fierro, A.; Sator, N. *J. Phys.: Condens. Matter* **2004**, *16*, S4831–S4839.
- (19) Imperio, A.; Reatto, L. *J. Phys.: Condens. Matter* **2004**, *16*, 3769.
- (20) Mossa, S.; Sciortino, F.; Tartaglia, P.; Zaccarelli, E. *Langmuir* **2004**, *20*, 10756–10763.
- (21) Kumar, A.; Wu, J. *Colloids Surf. A* **2004**, *247*, 145.
- (22) Wu, D.; Chandler, D.; Smit, B. *J. Phys. Chem.* **1992**, *96*, 4077–4083.
- (23) Deem, M. W.; Chandler, D. *Phys. Rev. E* **1994**, *49*, 4276–4285.
- (24) Cates, M. E.; Candau, S. J. *J. Phys.: Condens. Matter* **1990**, *2*, 6869–6892.
- (25) Muratov, C. B. *Phys. Rev. E* **2002**, *66*, 066108.
- (26) Tarzia, M.; Coniglio, A. *condmat/0506485*, 2005.
- (27) Sear, R. P.; Chung, S.; Markovich, G.; Gelbart, W. M.; Heath, J. R. *Phys. Rev. E* **1999**, *59*, 6255.
- (28) Lai, S. K.; Ma, W. J.; van Megen, W.; Snook, I. K. *Phys. Rev. E* **1997**, *56*, 766–769.
- (29) Lai, S. K.; Wang, G. F. *Phys. Rev. E* **1998**, *58*, 3072–3082.
- (30) Bosse, J.; Wilke, S. D. *Phys. Rev. Lett.* **1998**, *80*, 1260–1263.
- (31) Wang, G. F.; Lai, S. K. *Phys. Rev. Lett.* **1999**, *82*, 3645–3648.
- (32) Bernal, J. D. *Proc. Royal Soc. (London) A* **1964**, *299*, 280.
- (33) Previous literature on simulations of gelation processes includes, among others, refs 57–62.
- (34) Vliegthart, G. A.; Lodge, J.; Lekkerkerker, H. N. W. *Physica A* **1999**, *263*, 378.
- (35) In ref 7, the parameter  $A$  was estimated as  $30k_B T$ . However, this value is too high, and the potential is always positive at the considered  $\phi_p$  values. Thus, we chose the value of  $10k_B T$ .
- (36) Allen, M.; Tildesley, D. *Computer simulation of Liquids*; Oxford University Press: Oxford, England, 1989.
- (37) Torquato, S. *Random Heterogeneous Materials: Microstructure and Macroscopic Properties*; Springer-Verlag: New York, 2002.
- (38) Stauffer, D.; Aharony, A. *Introduction to Percolation Theory*, 2nd ed.; Taylor and Francis: London, 1992.
- (39) Coniglio, A.; DeAngelis, U.; Forlani, A. *J. Phys. A: Math. Gen.* **1977**, *10*, 1123–1139.
- (40) Chiew, Y. C.; Glandt, E. D. *J. Phys. A: Math. Gen.* **1983**, *16*, 2599–2608.
- (41) Chiew, Y. C.; Stell, G.; Glandt, E. D. *J. Chem. Phys.* **1985**, *83*, 761–767.
- (42) Stell, G. *J. Phys.: Condens. Matter* **1996**, *8*, A1–A17.
- (43) Groenewold, J.; Kegel, W. *J. Phys.: Condens. Matter* **2004**, *16*, S4877–S4886.
- (44) Steinhardt, P. J.; Nelson, D. R.; Ronchetti, M. *Phys. Rev. B* **1983**, *28*, 784.
- (45) Zaccarelli, E.; Sciortino, F.; Tartaglia, P. *J. Phys.: Condens. Matter* **2001**, *16*, 4849.
- (46) Zaccarelli, E.; Buldyrev, S. V.; La Nave, E.; Moreno, A. J.; Saika-Voivod, I.; Sciortino, F.; Tartaglia, P. *Phys. Rev. Lett.* **2005**, *94*, 218301.
- (47) Nicolai, T.; Urban, C.; Schurtenberger, P. *J. Colloid Interface Sci.* **2001**, *240*, 419–424.
- (48) Pouzot, M.; Nicolai, T.; Durand, D.; Benyahia, L. *Macromolecules* **2004**, *37*, 614–620.
- (49) Renard, D.; Axelos, M. A. V.; Lefebvre, J.; Boue, F. *Biopolymers* **1995**, *39*, 149–159.
- (50) Manno, M.; San Biagio, P. L.; Palma, M. U. *Proteins: Struct., Funct. Bioinf.* **2004**, *55*, 169–176.
- (51) Ruzicka, B.; Zulian, L.; Ruocco, G. *Phys. Rev. Lett.* **2004**, *93*, 258301.
- (52) Bordi, F.; Cametti, C.; Gili, T.; Gaudino, D.; Sennato, S. *Bioelectrochemistry* **2003**, *59*, 99–106.
- (53) F. Bordi.; Cametti, C.; Diociaiuti, M.; Gaudino, D.; Gili, T.; Sennato, S. *Langmuir* **2004**, *20*, 5214–5222.
- (54) Sennato, S.; Bordi, F.; Cametti, C. *J. Chem. Phys.* **2003**, *121*, 4936–4940.
- (55) Sennato, S.; Bordi, F.; Cametti, C. *Europhys. Lett.* **2004**, *68*, 296–302.
- (56) Bordi, F.; Cametti, C.; Sennato, S. *Chem. Phys. Lett.* **2005**, *409*, 134.
- (57) Bos, M. T. A.; vanOpheusden, J. H. *J. Phys. Rev. E* **1996**, *53*, 5044.
- (58) Lodge, J. F. M.; Heyes, D. M. *J. Chem. Soc., Faraday Trans.* **1997**, *93*.
- (59) Lodge, J. F. M.; Heyes, D. M. *Phys. Chem. Chem. Phys.* **1999**, *1*, 2119.
- (60) Hütter, M. *J. Colloid Interface Sci.* **2000**, *231*, 337.
- (61) Del Gado, E.; Fierro, A.; de Arcangelis, L.; Coniglio, A. *Europhys. Lett.* **2003**, *63*, 1.
- (62) Zaccarelli, E.; Sciortino, F.; Buldyrev, S. V.; Tartaglia, P. In *Unifying Concepts in Granular Media and Glasses*; Coniglio, A., Fierro, A., Hermann, H., Nicodemi, M., Eds.; Elsevier: Amsterdam, 2004; pp 181–194.